

Ballistic electron microscopy and spectroscopy of metal and semiconductor nanostructures

W. Yi, A.J. Stollenwerk, V. Narayanamurti*

School of Engineering and Applied Sciences, Harvard University, Cambridge, MA 02138, United States

ARTICLE INFO

Article history:

Accepted 23 January 2009
editor: W.H. Weinberg

Keywords:

Ballistic transport
Tunneling microscopy
Semiconductor heterostructures
Spintronics
Electroluminescence
Organic materials

ABSTRACT

Ballistic electron emission microscopy (BEEM) and its spectroscopy utilize ballistic transport of hot carriers as a versatile tool to characterize nanometer-scale structural and electronic properties of metallic and semiconducting materials and their interfaces. In this review, recent progress in experimental and theoretical aspects of the BEEM technique are covered. Emphasis is drawn to the development of BEEM in several emerging fields, including spin-sensitive hot-carrier transport through ferromagnetic thin films and multilayers, hot-electron spectroscopy and imaging of organic thin films and molecules, and hot-electron induced electroluminescence in semiconductor heterostructures. A brief discussion on BEEM of cross-sectional semiconductor heterostructures and advanced insulator films is also included.

© 2009 Elsevier B.V. All rights reserved.

Contents

1. Introduction.....	170
1.1. BEEM transport model.....	170
1.2. BEEM resolution.....	170
2. Magnetic thin films.....	171
2.1. Unpolarized ballistic electron transport.....	172
2.2. Spin-polarized ballistic electron transport.....	172
2.2.1. STM-based techniques.....	172
2.2.2. Planar tunneling techniques.....	174
2.3. Spin-polarized ballistic hole transport.....	176
3. Organic thin films and molecules.....	177
3.1. BEEM of buried organics.....	177
3.1.1. Barrier heights at metal–organic interfaces.....	177
3.1.2. Organic modified metal–semiconductor interfaces.....	178
3.2. BEEM of adsorbate organic molecules.....	179
4. Hot-electron luminescence.....	179
4.1. STM luminescence.....	181
4.1.1. Metal–metal junctions.....	181
4.1.2. Metal–semiconductor junctions.....	181
4.1.3. Heterojunction devices.....	182
4.2. BEEM luminescence.....	182
4.2.1. Bipolar collector.....	182
4.2.2. Fundamental and technical challenges.....	182
4.2.3. Unipolar collector.....	184
5. Cross-sectional BEEM.....	185
5.1. Quantum-size effect.....	186

* Corresponding address: School of Engineering and Applied Sciences, Harvard University, 29 Oxford Street, Pierce Hall 217A, Cambridge, MA 02138, United States. Tel.: +1 617 495 5829; fax: +1 617 496 5264.

E-mail address: venky@seas.harvard.edu (V. Narayanamurti).

5.2. Lateral resolution.....	187
6. Advanced insulator films.....	187
7. Conclusion.....	189
Acknowledgments.....	189
References.....	189

1. Introduction

Electron and hole transport is of great interest for the design of electronic devices. The continuing trend of device miniaturization requires a better understanding of the fundamental physics of this phenomenon on the nanometer scale. The invention of the scanning tunneling microscope (STM) by Binnig and Rohrer in 1981 has made it possible to perform both spectroscopy and imaging of surfaces on the atomic scale [1,2]. Ballistic electron emission microscopy (BEEM) is a three-terminal configuration of STM that allows the characterization of electron transport through materials and material interfaces on the nanometer scale [3,4]. In BEEM, hot electrons with extra kinetic energies up to several electron volts (eV) are injected from a STM tip (emitter) across a vacuum tunneling gap into a thin metal (base) layer that forms a Schottky contact on a semiconductor (collector) substrate (see Fig. 1). Those electrons with the appropriate energy and momentum distribution can traverse the base ballistically over the Schottky barrier into the collector.

First introduced in 1988, BEEM was initially used to study properties of various metal–semiconductor (m–s) systems such as Schottky barriers, interface band structure, hot-electron attenuation lengths and scattering properties of overlying metal films [3,4]. The field of BEEM quickly extended to buried semiconductor heterostructures including heterojunction band offsets, hot-carrier transport and resonant tunneling through double barrier and superlattice heterostructures. Further research was also performed on low-dimensional nanostructures such as quantum wires and quantum dots, as well as imaging buried structural defects such as dislocations and point defects [5–7]. BEEM has also been applied to study local transport properties through oxides in metal–insulator–semiconductor (MIS) structures [8–11].

A few excellent review articles on different aspects of BEEM have been published. Early BEEM research was reviewed in Refs. [5,12], BEEM on buried semiconductor heterostructures was discussed in detail in Ref. [6] and a comparative review of BEEM and hot-electron transistors (HET) can be found in Ref. [7]. The purpose of the present article is not to give a broad survey of the established areas in BEEM. Instead, the goal is to focus on a few emerging fields in which BEEM has made significant progress over the last few years or has demonstrated its promise as the appropriate characterization tool.

The present review is structured as follows: Section 2 reviews spin-sensitive hot-electron transport and BEEM research in magnetic thin films and multilayers; Section 3 reviews BEEM on organic materials; Section 4 reviews photon emission phenomena in BEEM and related luminescent hot-electron devices; and finally, Section 5 reviews several other promising areas including BEEM of cross-sectional semiconductor heterostructures and advanced insulator films.

1.1. BEEM transport model

The spectral shape of the BEEM current through m–s interfaces and semiconductor heterostructures can be derived from quantum mechanics and a detailed knowledge of semiconductor band structures. Two prevailing theoretical models, the Bell–Kaiser (BK) model and the Ludeke–Prietsch (LP) model, have been developed to describe the BEEM spectrum near the threshold region. They are

both based on a planar tunneling formalism and the assumption of transverse momentum conservation at the m–s interface. The LP model includes the energy-dependent electron attenuation in the metal base layer and quantum mechanical transmission (QMT) at the m–s interface. Both models give a power-law behavior of the near-threshold BEEM current as a function of the extra kinetic energy,

$$I_C \sim (eV_{tip} - \phi_S)^\alpha, \quad (1)$$

where e is the electron charge, V_{tip} is the tip-to-base bias and ϕ_S is the Schottky barrier height. The scaling exponent, α differs slightly for the BK ($\alpha = 2$) and LP ($\alpha = 2.5$) models. It was found that near the threshold regime (up to ~ 200 meV above the threshold), no quantitative difference between the BK and LP models can be resolved beyond the experimental error and both of them give a reasonably good fit to the experimental data. The BK model is most frequently used due to its simplicity. Deviations from this model at higher V_{tip} occur due to mechanisms including bias-dependent tunnel current distribution, scattering in the metal base and impact ionization in the semiconductor collector.

A more generalized description of BEEM must take into consideration the four distinct regions shown in Fig. 2. (1) The tunneling probability, $D(E_z)$ for an electron from the STM tip to the metal base; (2) the hot-electron transmission, $R(E)$ through the metal base characterized by an attenuation factor $R = \text{constant}$ (BK) or $R(E) = \exp[-d/\lambda(E)]$ (LP), where d is the thickness of the base and $\lambda(E)$ is the energy-dependent attenuation length; (3) the transmission probability, $C(E)$ across the m–s interface, which is either approximated as a step function (BK) or $C(E) \sim \sqrt{\frac{2m^*}{\hbar^2}(E - \phi_S) - k_{\parallel}^2}$ (LP), where m^* is the electron effective mass in the semiconductor, and k_{\parallel} is the transverse component of electron momentum (parallel to the interface); (4) the transmission probability, $S(E)$ across the semiconductor heterostructure, first introduced by Smith and Kogan (SK model) [13]. Steps (3) and (4) can be combined into an overall transmission coefficient, $T(E)$ across the m–s interface and the buried heterostructure with a transfer matrix method [7]. In these terms, the total collector current in the extended BK model can be written as [7]

$$I_C(V_{tip}) = RI_{tip} \frac{\int_{E_z^{\min}}^{\infty} dE_z D(E_z) T(E_z) \int_0^{E_{\parallel}^{\max}} dE_{\parallel} [f(E) - f(E + eV_{tip})]}{\int_0^{\infty} dE_z D(E_z) \int_0^{\infty} dE_{\parallel} [f(E) - f(E + eV_{tip})]}, \quad (2)$$

where I_{tip} is the tip tunnel current. The integral limits $E_z^{\min} = E_f - eV_{tip} + \phi_S$ and $E_{\parallel}^{\max} = \frac{m^*}{m_0 - m^*}(E_z - E_f + eV_{tip} - \phi_S)$ are due to the conservation of the total energy and transverse momentum of electrons at the m–s interface. Here, E_f is the Fermi energy and m_0 is the free electron mass.

1.2. BEEM resolution

Transverse momentum conservation at the m–s interface has been traditionally used to account for BEEM resolution. Due to the much smaller electron effective mass in the semiconductor and the potential step (Schottky barrier) at the interface, the transverse momentum conservation implies that an electron refraction effect exists at the interface. As a result, only electrons with their angle of incidence smaller than a critical acceptance angle can be

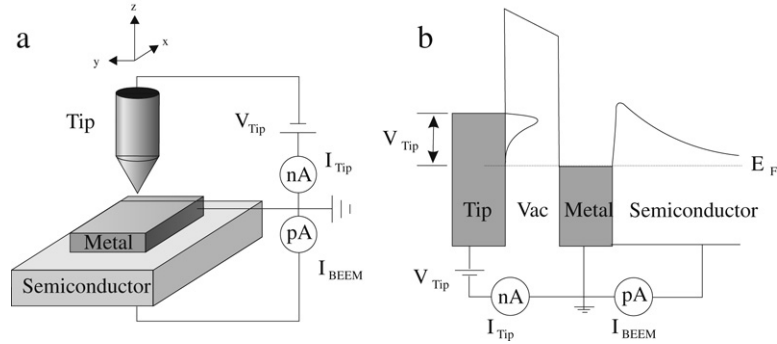


Fig. 1. (a) Schematic diagram of the experimental setup for BEEM and (b) the corresponding energy band diagram.

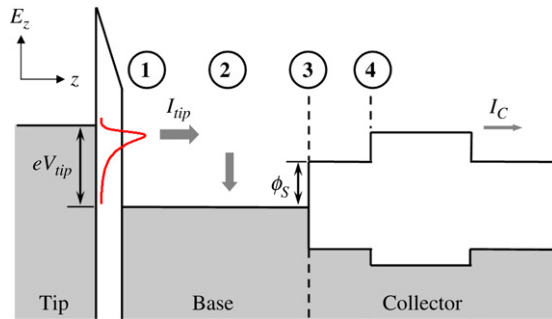


Fig. 2. Schematic of hot-carrier transport phenomena involved in theoretical modeling of BEEM. Four distinct transport regions exist in this system. (1) Tunneling from the STM tip to the metal base, (2) propagation (attenuation) in the metal base, (3) transmission at the m–s interface and (4) transmission at the buried heterojunction interface.

collected into the semiconductor. Those scattered electrons with a larger angle of incidence will be reflected at the interface and not contribute to the collector current. The critical acceptance angle, θ_c is obtained from [3]

$$\sin^2(\theta_c) = \frac{m^* eV_{tip} - \phi_S}{m_0 eV_{tip} + E_f}. \quad (3)$$

For the Au–GaAs interface, the calculated θ_c is only a few degrees. Since hot electrons initially tunneling into the base are highly focused in the forward direction, the small acceptance angle essentially acts as a filter that allows only ballistic electrons to be collected. Scattering in the base layer usually does not deteriorate the lateral resolution, but rather less collector current is measured. This is in large contrast to a solid-state all-semiconductor HET device in which no such large effective-mass mismatch exists.

The transverse momentum conservation originates from the translational symmetry in the plane; therefore, for nonepitaxial m–s interfaces transverse momentum may not be strictly conserved. For example, BEEM on Au/GaAs(001) found that the contribution from the L valley, consisting of states with substantial transverse wavevectors, is actually much greater than that from the Γ valley [14]. To explain this discrepancy, the m–s interface induced scattering (MSIS) model was proposed [15]. This model includes the anisotropic nature of the electron effective mass. It was found that scattering at the m–s interface can redistribute the injected electron flux so that valleys with zero interface transverse wavevector are not preferentially weighted. The BEEM data on Au/Si and Au/GaAs systems are adequately described only in the strong scattering limit. This was further confirmed by secondary-derivative BEEM spectra on Au/GaAs/Al_xGa_{1-x}As single-barrier systems [16].

In general, interfacial scattering is undesirable because it deteriorates the spatial resolution of BEEM. However, for specific

hot-electron devices, such as integrated thermionic energy converters, complete nonconservation of transverse momentum is preferred to achieve the highest possible thermoelectric power factors [17,18].

Experimentally, the observed lateral resolution of BEEM has been found to be as small as 1 nm at the m–s interface after hot electrons traverse a Au base with a thickness of 10 nm [6]. BEEM imaging on epitaxially-grown CoSi₂/Si structures have proven the ability to obtain atomic resolution [19]. This was attributed to an electron focusing effect resulting from the silicide band structure.

2. Magnetic thin films

The study of magnetic thin films with BEEM is partially fueled by the great success of spintronic (spin-based electronics) devices which rely heavily on the intrinsic properties of magnetic thin films. Spintronic technology exploits the charge as well as the spin degree of freedom of the electron. These devices have the potential of being faster and consuming less energy than conventional devices [20–22]. Past research of magnetic thin films has led to the development of successful spintronic devices. Most notable was the discovery of giant magnetoresistance (GMR) [23,24]. GMR is the large change in electrical resistance of certain multilayered structures in the presence of an external magnetic field. The application of this phenomenon in hard drive read heads resulted in a dramatic increase in storage capacity. The mechanism that makes magnetoresistive devices possible is spin dependent scattering in ferromagnetic (FM) materials. Spin dependent scattering arises from the imbalance in the density of states (DOS) between the spin-minority and spin-majority carriers due to the difference in the energy associated with the two spin species of carriers in the presence of a magnetic field [25]. Minority electrons have a larger number of empty states to decay into than do the majority electrons. Thus, according to Fermi's golden rule, the probability of scattering is greater for the minority electrons than for the majority. The difference in the DOS also creates an imbalance of spin electrons. This imbalance can be quantified in terms of the polarization, $P = (N_+ - N_-)/(N_+ + N_-)$, where N_+ is the number of majority electrons in the system and N_- is the number of minority electrons. When the DOS is composed entirely of electrons of one type of spin orientation that material is said to be 100% spin polarized.

The GMR spin valve consists of two FM metals sandwiching a non-FM metal. Changing the magnetic alignment of the two FM metals causes the DOS of the spin populations in one metal to change relative to the other. This causes a change in the resistance of the structure, a minimum resistance when the magnetic alignment is parallel (P) and a maximum resistance when it is anti-parallel (AP). The quality of a magnetoresistive device can be gauged by the magnetoresistance ratio (MR), defined as

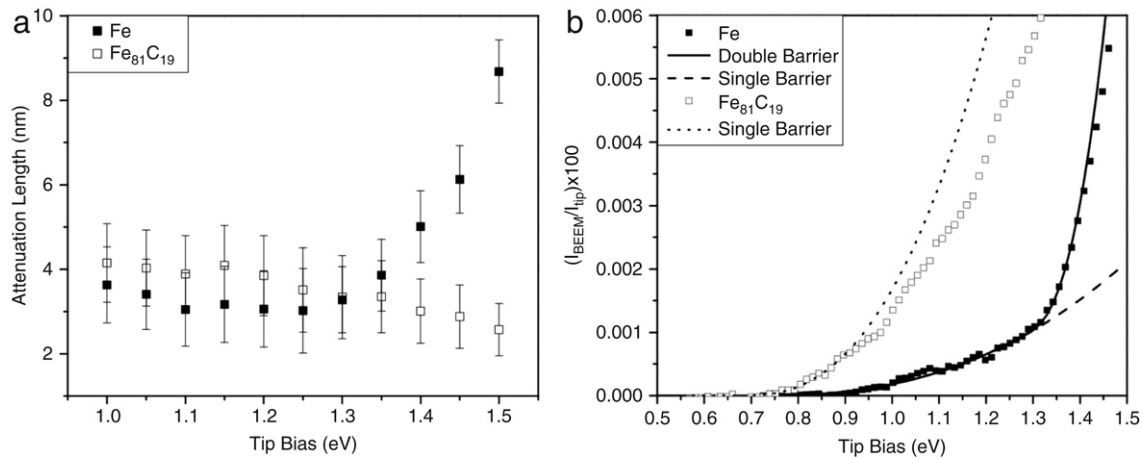


Fig. 3. (a) The ballistic attenuation lengths as a function of tip bias for Fe₈₁C₁₉/Si(001) and Fe/Si(001) Schottky diodes. (b) Examples of BEEM spectra obtained from these diodes. Note the second threshold voltage in the spectra of the Fe films at 1.29 eV corresponding to the sharp increase in the energetic dependence of its attenuation length seen in (a). Reprinted with permission from Ref. [33]. © 2006, American Physical Society.

$(R_P - R_{AP})/(R_{AP}) \times 100$, where R_P is the parallel resistance and R_{AP} is the anti-parallel resistance. Typically, the percentage change in MR for a GMR read head is 10%–20%, which is much greater than the 3% achieved in anisotropic magnetoresistive read heads used previously. Currently, GMR devices are being superseded by magnetic tunneling junction (MTJ) devices for hard drive read heads. MTJs use an insulator as the spacer layer between the FM metals and exhibit an even higher MR of 20%–30% [26–28].

The following section on spin dependent transport is limited by the scope of this review article. An enormous amount of research has been performed in the field of spintronics, both experimental and theoretical. The interested reader should refer to the reviews that have been previously published (see for example Refs. [20,29–31]).

2.1. Unpolarized ballistic electron transport

Before understanding spin-polarized electron transport in magnetic thin films, it is first useful to examine hot-electron transport in a single FM layer without discrimination of their spin degree of freedom. One way to quantify hot-electron transport is by measuring the attenuation length, λ . This is done by measuring the BEEM current, I_C through a Schottky diode, as a function of metal thickness and tip bias. The effective attenuation length through the diode can then be obtained from

$$I_C(d, V_{\text{tip}}) = I_C(d = 0, V_{\text{tip}})e^{(-d/\lambda)}. \quad (4)$$

Here $I_C(d = 0, V_{\text{tip}})$ is a proportionality constant.

Recently, this method has been utilized on magnetic thin films such as Co, Fe, FeC, Ni and NiFe yielding ballistic attenuation lengths ranging from 0.3 to 4.1 nm at room temperature [32–35].

BEEM spectra acquired on MnSi/Si(001) Schottky diodes at 80 K displayed two threshold voltages at 0.71 ± 0.01 eV and 0.86 ± 0.02 eV [36]. The second threshold is attributed to the existence of an additional conduction band minimum (CBM) in the band structure at the MnSi/Si(001) interface. This was unexpected since additional CBM is not present in the bulk Si band structure in this energy range [37], nor are they observed in BEEM experiments using more ideal metals such as Au. Additional CBMs were theoretically predicted in the NiSi₂/Si(001) system but have not been observed in experimental BEEM studies, possibly due to scattering in the silicide [38–40]. A study of Au/Fe/Si(001) Schottky diodes at 80 K also found an additional threshold voltage in the BEEM spectra occurring at 1.29 ± 0.04 eV [33]. The additional CBM

associated with the second threshold was previously predicted and attributed to metal induced gap states (MIGS) resulting from the poor coordination of dangling d bonds at the Fe interface layer with the Si [41]. It is unlikely that this extra threshold is from a thin FeSi alloyed layer since there was no annealing step after deposition and the bandgap of such a layer would only be 0.13 eV [42]. The addition of 19% C to the Fe films was found to suppress the additional threshold voltage. The addition of C possibly eliminates the dangling bonds of Fe as well as the MIGS.

The energetic dependence of the attenuation length measured on Au/Fe/Si(001) and Au/FeC/Si(001) Schottky diodes is shown in Fig. 3(a). The attenuation lengths measured on the Au/FeC/Si(001) diodes decrease monotonically with energy in this energy range, consistent with electron–electron scattering. In contrast, the Au/Fe/Si(001) diodes exhibited a dramatic increase in the effective attenuation length at approximately 1.3 eV. This increase coincides with the onset of the second threshold voltage in the Au/Fe/Si(001) BEEM spectra at 1.29 eV seen in Fig. 3(b). The CBM associated with the second threshold voltage has a larger number of available transverse momentum states with greater transverse momentum than the CBM associated with the Schottky threshold. The larger number of available states makes the BEEM current less sensitive to electrons elastically scattered in the Fe film, causing an increase in the effective attenuation length in these diodes. A second threshold voltage was not seen in the Au/FeC/Si(001) Schottky diodes (see Fig. 3(b)).

2.2. Spin-polarized ballistic electron transport

The past success of BEEM to study non-polarized hot-electron transport makes it an ideal technique to study spin-polarized electron transport. There are two different categories of BEEM techniques: the first is based on the STM setup, while the second makes use of planar tunneling devices. This section will describe how both of these methods have been modified to study spin-polarized transport as well as some of the more significant results.

2.2.1. STM-based techniques

In order to take advantage of the nanoscale positioning of the STM scanner, Rippard et al. modified the BEEM technique to perform ballistic electron magnetic microscopy (BEMM) [43]. In BEMM, a thin film stack is grown on a semiconductor substrate consisting of two FM metal layers decoupled by a non-FM spacer layer. Using the BEEM setup, electrons are injected from the STM

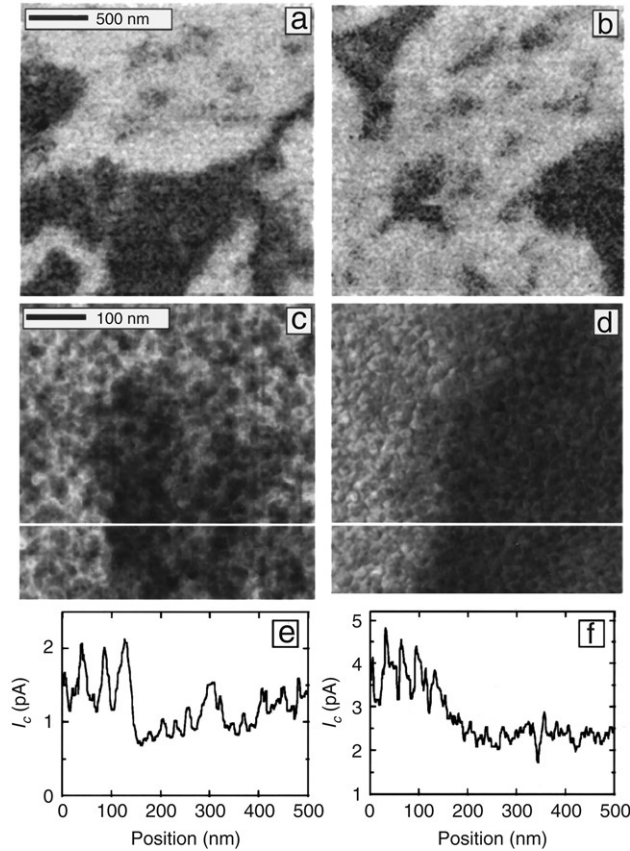


Fig. 4. BEMM image of sputtered Au/Cu/Co/Cu/Co/Cu/Au structures on Si(111) at $H = 30$ Oe (a) and after H has been reduced to 0 Oe (b). 500×500 nm² BEMM images of similar (c) sputtered and (d) evaporated films. The cross-sectional plots of the white lines in (c) and (d) are shown below their respective images in (e) and (f). $V_{tip} = 1.5$ eV and $I_{tip} = 4$ nA. Reprinted with permission from Ref. [44]. © 2000, American Institute of Physics.

tip into the first FM metal where they become polarized. This occurs due to an asymmetry in the scattering rate of the two spin species in the film as well as spin dependent reflections at the interface. Similar to the GMR effect, the amount of spin dependent scattering in the second FM metal depends on its magnetic alignment with the first. Essentially, the first FM metal acts as the polarizer while the second FM metal plays the part of the analyzer. This effect gives BEMM magnetic contrast and has provided some interesting images of magnetic domains on Co/Cu/Co [43,44] as well as on Co/Cu/NiFe [45] stacks.

Images in Fig. 4 demonstrate the ability of BEMM to image magnetic domains of Au/Cu/Co/Cu/Co/Cu/Au structures on Si(111) at room temperature. These structures typically exhibited domain walls with widths of 100–200 nm. Fig. 4(a) and (b) show how the domains change as the magnetic field is reduced from 30 to 0 Oe on sputtered films. The transition of these domains from P alignment to AP alignment was found to occur over a variety of lengths from ~ 10 nm to several hundred nanometers, as seen in the sputtered films (Fig. 4(c)) and the corresponding line scan in (e)) and in the evaporated films (Fig. 4(d)) and its corresponding line scan in (f)), respectively.

In addition to magnetic imaging, BEMM can also be utilized to perform spectroscopy. Fig. 5(a) demonstrates the change in the spectra with and without an applied external field of 26 Oe on a Au/NiFe/Cu/Co/GaAs(001) sample at room temperature using a tunneling current of 20 nA. By measuring the BEMM current as a function of applied external field, it is possible to measure a BEMM hysteresis loop [45,46]. The hysteresis occurs due to

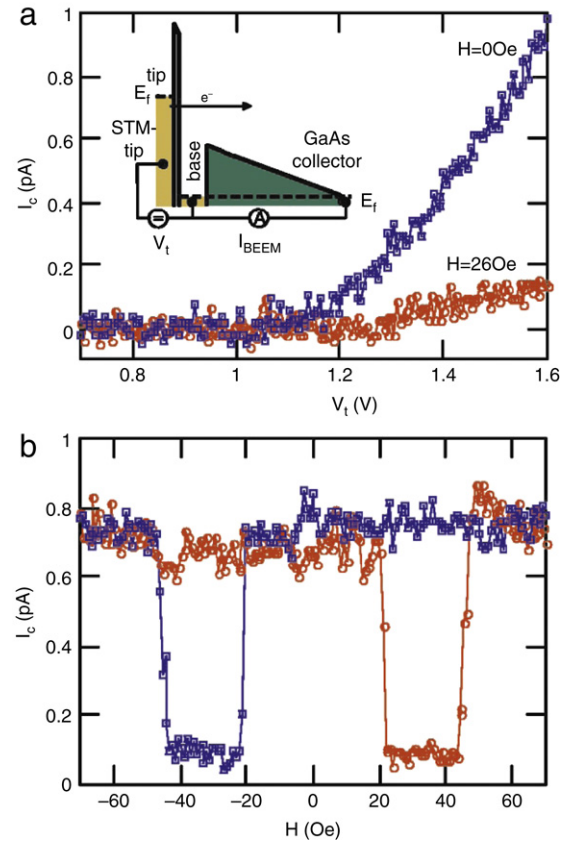


Fig. 5. (a) BEMM spectra recorded on Au/NiFe/Cu/Co/GaAs(001) using a tunneling current of 20 nA at $H = 0$ Oe and $H = 26$ Oe corresponding to parallel and anti-parallel alignment, respectively. (b) Collector current measured as a function of magnetic field for $V_{tip} = 1.5$ eV and $I_{tip} = 20$ nA at room temperature. Reprinted with permission from Ref. [45]. © 2004, American Institute of Physics.

a difference in the coercivity of the two FM metals in the trilayer stack. An example of such a hysteresis loop is shown in Fig. 5(b) for Au/NiFe/Cu/Co/GaAs(001). For both polarities the BEMM current reaches a minimum between ~ 20 and ~ 40 Oe. As the field increases beyond 40 Oe, the two FM layers are forced into P alignment resulting in a higher BEMM current. The magnetocurrent (MC) can be determined from such hysteresis loops. The MC is defined in terms of the BEMM current in P and AP alignment as $(I_{C,P} - I_{C,AP}) / (I_{C,AP}) \times 100$. Various types of spin valves have been studied in this manner yielding MCs ranging from 400%–600% [45,46].

The effective spin dependent attenuation lengths have been determined by measuring the BEMM current in P and AP alignment on Co/Cu/Co/Cu/Au/Si(111) Schottky diodes as a function of the thickness of the second Co layer [47]. This was accomplished in a similar manner as the unpolarized attenuation lengths; however, Eq. (4) is insufficient to describe a two current system. In order to properly model the BEMM current in P and AP alignment, the following equations are used [47]:

$$I_{C,P} = I_0 [f_+ T_{0+} T_{i+}^* T_{o+}^* e^{-(d_1/\lambda_+)} e^{-(d_2/\lambda_+)} + f_- T_{0-} T_{i-}^* T_{o-}^* e^{-(d_1/\lambda_-)} e^{-(d_2/\lambda_-)}], \quad (5)$$

$$I_{C,AP} = I_0 [f_+ T_{0+} T_{i-}^* T_{o-}^* e^{-(d_1/\lambda_+)} e^{-(d_2/\lambda_-)} + f_- T_{0-} T_{i+}^* T_{o+}^* e^{-(d_1/\lambda_-)} e^{-(d_2/\lambda_+)}]. \quad (6)$$

Here I_0 is the overall scaling factor, $f_{+(-)}$ is the fraction of majority (minority) electrons in the initial tunneling current due to the

splitting of the spin dependent DOS in the first Co film, $\lambda_{+(-)}$ is the effective majority (minority) attenuation length in the Co films, $T_{o(i)+(-)}$ is the transmission coefficient out of (into) a Co layer for the majority (minority) electrons, $d_{1(2)}$ is the Co thicknesses of the first (second) layer. The * indicates the second Co layer beneath the Cu film. Fitting these equations to the data, the effective spin dependent attenuation lengths for Co at 300 K were extracted yielding values of $\lambda_+ = 2.1 \pm 0.1$ nm and $\lambda_- = 0.83 \pm 0.08$ nm at a tip bias of $V_{tip} = 1.5$ eV. These values indicate that the minority electrons are being scattered at a rate approximately 2.5 times greater than the majority electrons.

Spin flip scattering acts to randomize the spin orientation of a current. This process would tend to reduce the polarization of the current and have a detrimental effect on spintronic devices. Perrella et al. studied the change in polarization due to the effects of electron–electron scattering in the spacer layer of Co/Cu/Al/Cu/Co/Cu/Au/Si(111) Schottky diodes using previously measured attenuation lengths in Co [48]. Knowing the spin dependent attenuation lengths allows the polarization of ballistic electrons exiting the first Co to be calculated as a function of the film thickness from

$$P_{in} = \frac{e^{-d/\lambda_+} - \alpha e^{-d/\lambda_-}}{e^{-d/\lambda_+} + \alpha e^{-d/\lambda_-}}, \quad (7)$$

where α is a transmission coefficient for the first Co/Cu interface. The polarization of the current exiting the spacer layer can be determined by using the current measured in the P and AP alignments in the equation

$$P_{out} = \frac{e^{-d/\lambda_+} + \beta e^{-d/\lambda_-}}{e^{-d/\lambda_+} - \beta e^{-d/\lambda_-}} \left(\frac{I_{C,P} - I_{C,AP}}{I_{C,P} + I_{C,AP}} \right), \quad (8)$$

where β is a transmission coefficient for the second Cu/Co interface. The amount of electron–electron scattering was controlled by adjusting the O_2 content in the Al layer. Fig. 6(a) shows the polarization of the BEMM current coming out of the Cu/Al/Cu spacer layer as a function of O_2 dose at a tip bias of $V_{tip} = 2.0$ eV. The dashed line indicates the polarization of the electrons exiting the first Co film as well as the polarization of the BEMM current with no O_2 exposure. An obvious decrease in polarization is seen as the O_2 content (i.e. the amount of electron–electron scattering) increases. Fig. 6(b) shows the polarization out of the spacer layer as a function of the maximum BEMM current. The decrease in polarization with decreasing current provides direct evidence that scattering which causes a loss of signal also causes a loss of polarization.

Spin-polarized tunneling with STM was demonstrated nearly two decades ago utilizing an FM metal tip to inject spin-polarized carriers [49]. Recently, such tips were used in a three-terminal BEMM configuration to study spin-polarized ballistic transport through FM metal overlayers on semiconductor substrates [50]. This technique has the advantage of requiring only a single FM metal film grown on a semiconductor rather than a more complicated multilayered stack, greatly simplifying Eqs. (5) and (6),

$$\frac{I_{C,P}(AP)}{I_{tip}} = \frac{C_+}{2} (1 + (-)P_0) e^{-d/\lambda_+} + \frac{C_-}{2} (1 - (+)P_0) e^{-d/\lambda_-}. \quad (9)$$

Here P_0 is the initial polarization of the electrons tunneling from the FM tip and $C_{+(-)}$ takes into account the non-thickness dependent scattering (i.e. interface scattering) of majority (minority) electrons.

Thickness dependent BEMM using an Fe-coated Au tip was performed on Au/Fe/Si(001) Schottky diodes at 80 K yielding attenuation lengths of 2.5 ± 0.3 nm for the majority and 1.8 ± 0.2 nm for the minority electrons at a tip bias of 1.5 eV. Similar to the unpolarized case [33], the majority attenuation length exhibited a substantial increase after the onset of the second

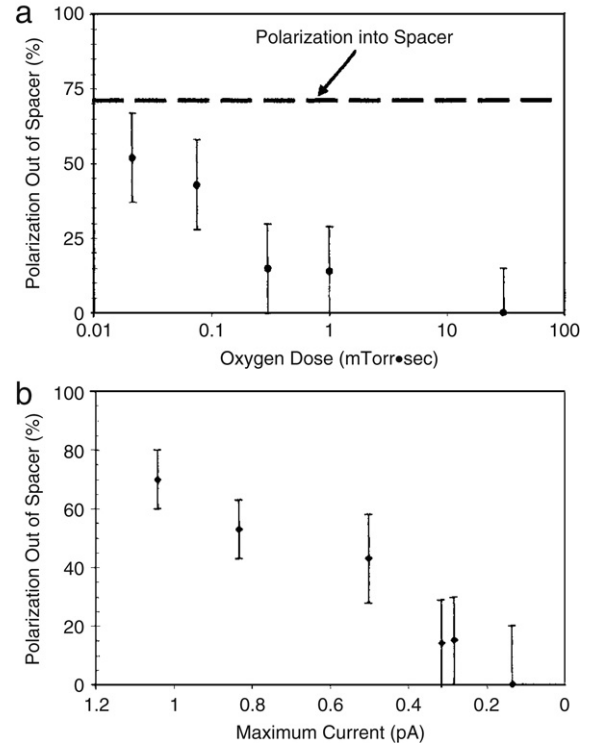


Fig. 6. (a) The electron polarization exiting the spacer layer of Co/Cu/Al/Cu/Co/Cu/Au/Si(111) samples as a function of the oxygen dose in the Al film. The horizontal line at 71% indicates the polarization entering the spacer layer as well as the polarization measured when the spacer layer is entirely Cu or when the Al is not exposed to oxygen. (b) The polarization exiting the spacer layer as a function of the maximum current at a tip bias of 2.0 eV. Reprinted with permission from Ref. [48]. © 2005, American Institute of Physics.

threshold voltage at 1.29 eV. This was also observed in the minority electrons to a lesser degree. The increased attenuation length beyond the second threshold is due to the collection of electrons with large transverse momentum. Minority electrons that undergo high elastic scattering rate in the metal have a broader momentum distribution at the m–s interface. Therefore the effect of increased transmission is less prominent.

2.2.2. Planar tunneling techniques

An alternative to STM-based BEMM techniques is to use planar tunneling devices such as the metal-based hot-electron transistor. Rather than injecting electrons by means of a STM tip, the hot electron transistor uses a planar solid-state tunnel junction to inject hot electrons ballistically through a metal base layer into a semiconductor collector. The magnetic tunneling transistor (MTT) is a modified hot-electron transistor that utilizes an MTJ to inject spin-polarized electrons ballistically through an FM metal base layer into a semiconductor collector [51,52].

Though incapable of magnetic imaging like its BEMM counterpart, MTTs are capable of performing spectroscopic analysis of FM metals. Thickness dependent studies of NiFe in Ta/IrMn/CoFe/Al₂O₃/NiFe/GaAs(001) MTTs at 77 K have given values of 6.7 ± 0.26 nm for the majority and 1.3 ± 0.1 nm for the minority electron attenuation lengths [53]. Extrapolation of the MC measured in these samples reveals that it approaches zero at zero thickness. This indicates that spin dependent scattering between the NiFe and the GaAs(001) is negligible. In a similar experiment, when CoFe was used in place of NiFe, it was uncertain if the MC went to zero, making it impossible to rule out spin dependent scattering at the interface [53].

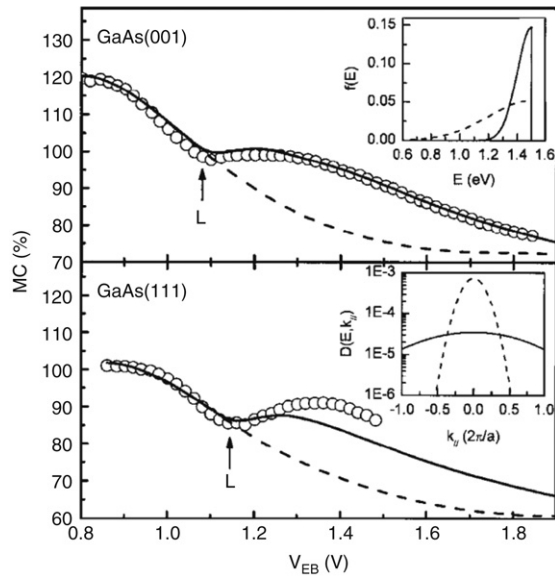


Fig. 7. Bias dependence of the MC for Ta/IrMn/CoFe/Al₂O₃/CoFe on both GaAs(001) (top) and GaAs(111) (bottom) MTTs. The solid lines represent the calculated MC assuming a large angular distribution. The dashed lines represent the same calculation except for a smaller angular distribution. The arrows indicate the onset of electron transmission into the GaAs *L* conduction band valley. The upper and lower insets show a narrow and broad electron energy distribution function and electron angular distribution function at $V_{EB} = 1.5$ eV, respectively. Reprinted with permission from Ref. [54].

© 2003, American Physical Society.

The MC of Ta/IrMn/CoFe/Al₂O₃/CoFe/GaAs MTTs on both GaAs(001) and GaAs(111) substrates seen in Fig. 7 exhibit a nonmonotonic dependence on the emitter bias at 77 K. At an emitter bias of approximately $V_{EB} = 1.1$ eV both structures display a change in the energetic dependence of the MC as the *L* conduction band opens. This dependence has also been seen on other GaAs-based MTTs and indicates that the band structure of the metal/GaAs interface is affecting spin transport in these devices [54,55]. This behavior can be predicted using the model developed for BEEM [56,15,57]. Taking spin dependent effects into account, the collector current can be written as [54]

$$\begin{aligned}
 I_{C,P(AP)} = & I_E(0.5 + 0.5P_E)\exp(-d/\lambda_{+(-)}) \\
 & \times \int_{\phi_S}^{eV_{EB}} f_{+(-)}(E) \int D(E, k_{\parallel})T(E, k_{\parallel})dk_{\parallel}dE \\
 & + I_E(0.5 - 0.5P_E)\exp(-d/\lambda_{-(-)}) \\
 & \times \int_{\phi_S}^{eV_{EB}} f_{-(-)}(E) \int D(E, k_{\parallel})T(E, k_{\parallel})dk_{\parallel}dE, \quad (10)
 \end{aligned}$$

where I_E is the tunnel current injected from the emitter into the base, P_E is the injection polarization, d is the thickness of the base layer, $\lambda_{+(-)}$ is the majority (minority) attenuation length in the base layer, ϕ_S is the Schottky barrier height, $f_{+(-)}$ is the distribution function for the majority (minority) electrons at the *m*-*s* interface, D is the angular distribution of the electrons due to scattering in the base layer, T is the transmission probability at the *m*-*s* interface, and k_{\parallel} is the momentum vector parallel to the sample surface. It should be noted that the attenuation lengths in this equation are not the effective attenuation lengths measured using BEEM, rather they are the attenuation lengths inside the FM metal base.

The upper inset of Fig. 7 shows the electron energy distribution for a large (dashed line) and small (solid line) amount of scattering, representative of the minority and majority electrons, respectively. Because the spin asymmetry is greatest for energies closest to eV_{EB} , the maximum MC collected through the narrow Brillouin

zone centered (Γ point) conduction band in GaAs is obtained when the electrons are collected with a minimum energy loss ($eV_{EB} \approx \phi_S$). As the emitter bias increases, inelastic scattering of electrons will be less likely to remove these electrons from the collector current, causing a decrease in the MC. The same is also true as electrons begin to access the *L* valley conduction band. The increase in the MC seen at $V_{EB} \approx 1.1$ eV indicates a large contribution to the current from electrons propagating in the *L* valley. The lower inset shows a broad (solid line) and narrow (dashed line) angular distribution. Because all or six out of eight *L* valley ellipsoids (for the GaAs(001) and GaAs(111) substrates, respectively) are centered at large transverse wavevectors, the large contribution of the *L* valley to the collector current can only be explained if the electrons have a large angular distribution at the CoFe/GaAs interface (solid lines). Indeed, when a narrow distribution is assumed, a monotonic dependence is seen (dashed lines). The slight difference in the shape of the emitter bias dependence of the MC on the GaAs(001) and GaAs(111) substrates is attributed to structural differences on the two different facets.

In general, MTTs have only exhibited a moderate MC of approximately 100% [53,58]. One notable exception is a modified MTT developed by Van Dijken et al. that uses a nonmagnetic tunneling junction to inject electrons into a GMR spin valve base [59]. This structure consists of Cu/Al₂O₃/NiFe/Cu/CoFe/GaAs(001) and exhibits a MC of more than 3400% at $V_{EB} \sim 0.8$ eV at 77 K. More important, from a device standpoint, was the large collector current (~ 7.5 μ A) measured at $V_{EB} = 2.5$ eV while still maintaining a MC of 670%. It is not expected that the MC would change significantly at room temperature since only a moderate MC temperature dependence has been observed [60].

The solid circles in Fig. 8(a) show the MC of this device as a function of FM layer thickness. The open circles show the corresponding effective transmission polarization at an emitter bias of $V_{EB} = 1.5$ eV. The effective transmission polarization is calculated from the MC by $P = \sqrt{MC/2 + MC}$. The rapid increase in transmission polarization occurs due to the relatively large asymmetry in the spin dependent scattering inside the FM layers. The saturation of the P at $\sim 95\%$ for FM layer thicknesses greater than 5 nm is an indication that the maximum polarization of this structure is limited by spin flip scattering events at the interfaces of the films.

The emitter bias dependence of the MC is shown in Fig. 8(b) for a structure with a 5 nm thick NiFe layer. At higher emitter biases inelastic scattering of electrons will be less likely to remove these electrons from the collector current, causing the decrease in the P with emitter bias. Fig. 8(c) and (d) depict the difference in the electron energy distribution for P and AP alignments of the FM metals.

Previous studies of spin transport inside semiconductors have been primarily limited to direct-bandgap semiconductors due to the need to measure the photon polarization after spin injection [61,62]. Recently, it has been shown that spin transport in Si can be studied electrically using modified MTTs [63–67]. These MTTs utilize an undoped single crystal Si spacer layer between two FM layers. The dependence of the collector current on the relative magnetization of the FM layers indicates that spin coherence is maintained in Si layers to at least 350 μ m. Spin precession in a perpendicular magnetic field was studied with these devices by measuring the oscillations in the collector current as a function of the applied magnetic field. The average spin transit time, τ is related to the period of these oscillations, $2B_{\pi}$ by $\tau = h/(2g\mu_B B_{\pi})$. Here, g is the electron spin g factor and μ_B is the Bohr magneton. Knowing the spin transit time allows the spin lifetime, T_1 to be calculated from the magnetocurrent using a simple exponential decay relationship,

$$MC/(MC + 2) \propto e^{-\tau/T_1}. \quad (11)$$

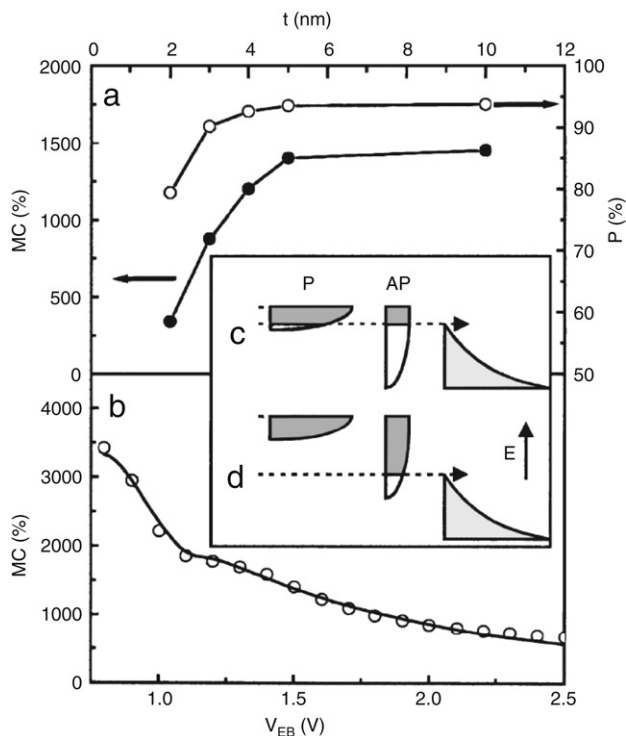


Fig. 8. (a) The FM layer (CoFe and NiFe) thickness dependence of the MC (solid circles) of Cu/Al₂O₃/NiFe/Cu/CoFe/GaAs(001) MTTs and the corresponding effective transmission polarization of the FM layers (open circles) for an emitter bias of 1.5 eV. (b) Emitter bias voltage dependence of the MC for a MTT with FM layer thickness of 5 nm (open circles). The solid line represents the theoretical fit. The difference in electron energy distribution for parallel and anti-parallel alignment of the base magnetic moments is illustrated for small (c) and large (d) emitter bias voltage. Reprinted with permission from Ref. [59]. © 2003, American Institute of Physics.

Shown in Fig. 9(a) is the normalized MC obtained from a MTT with a 350 μm Si spacer layer as a function of transit time at device temperatures ranging from 60 to 150 K. The transit times were determined from spin precession experiments in a perpendicular magnetic field. The solid lines represent fits to Eq. (11). The resulting spin lifetimes determined from these fits are plotted as a function of temperature in Fig. 9(b) as well as a comparison to Yafet's $T^{-5/2}$ power law for indirect-bandgap semiconductors [68]. These results show that this technique holds promise for studying spin injection in a wide variety of indirect-bandgap semiconductors.

2.3. Spin-polarized ballistic hole transport

While much research has been devoted to the study of spin-polarized electron transport in magnetic thin films using BEEM-based techniques, little work has been done to study spin-polarized holes. If holes are able to transverse interfaces without the loss of spin polarization then spintronic devices based on hole injection into p-type semiconductors can be realized. To this end, ballistic hole magnetic microscopy (BHMM) was developed to study spin hole transport [69]. In BHMM, hot holes are injected from a STM tip into a spin valve structure on a p-type semiconductor using a positive tip bias. In this manner the amount of hole current can be measured in P and AP alignment.

The top panel of Fig. 10 shows a clear change in the amount of hole current for P ($H = 100$ Oe) and AP ($H = -30$ Oe) alignment acquired at 150 K on Au/Co/Au/NiFe/Au/p-Si(001) Schottky diodes indicating that spin dependent scattering is occurring. This is further reinforced by the BHMM hysteresis loop shown in the

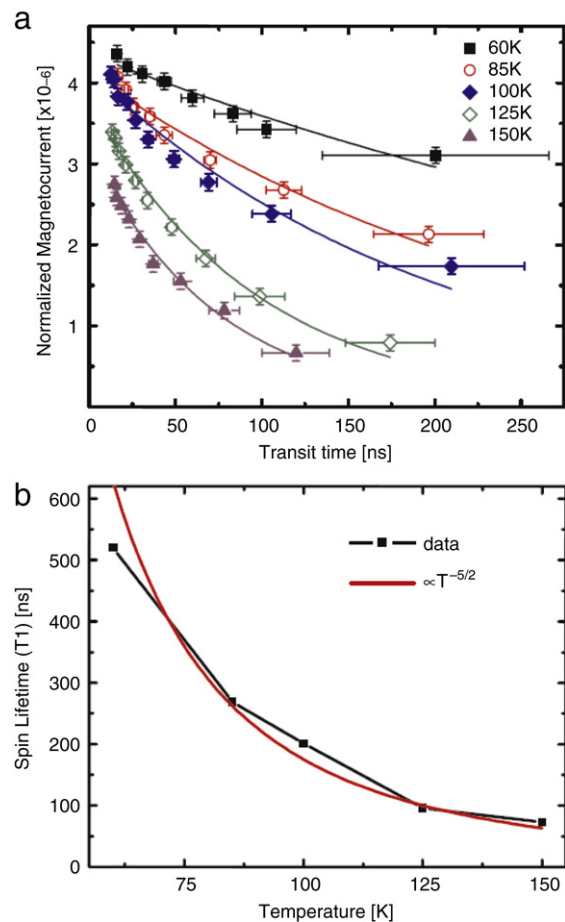


Fig. 9. (a) Fits of the normalized magnetocurrent using Eq. (11) to the spin transit time in a MTT with a 350 μm Si spacer layer. (b) The experimental spin lifetime as a function of device temperature compared to Yafet's $T^{-5/2}$ power law. Reprinted with permission from Ref. [65]. © 2007, American Physical Society.

bottom panel of Fig. 10, acquired at a tip bias of $V_{tip} = 2$ eV and a 10 nA hole injection current. This structure was found to exhibit a MC of 130%. The large dependence of the hole current on the magnetic alignment was unexpected for these samples, since there is little difference in the number of final states into which a hot hole in the majority and minority spin bands can decay just below the Fermi level in Co [69]. The spin dependent scattering is explained by taking into account the difference in group velocity in the states in which the two different spin holes can propagate [69]. The inset of Fig. 10 shows the partial density of *s*, *p* like states for Co in the face-centered-cubic (FCC) phase. The decrease in the majority states just below E_F results in a smaller velocity of these holes, increasing the time they spend in the FM metal. This in turn gives them more opportunities to undergo inelastic scattering. This hypothesis suggests that the current due to holes traveling in the minority band is greater than that of the majority band, the opposite of what is observed for electrons. It would be interesting if temperature dependence were studied.

To further complicate our understanding of spin-polarized holes, both negative and positive MCs were measured on NiFe/Al₂O₃/Co/Si p-type MTTs as a function of Co thickness as well as hole energy [70]. In many cases a crossover from negative to positive MC was measured for both thickness and emitter bias dependence. The measurement of a negative MC is consistent with the proposal that the current in Co due to holes traveling in the minority band is greater than those in the majority band [69]. It was found that the negative MC tended to occur in thinner Co films

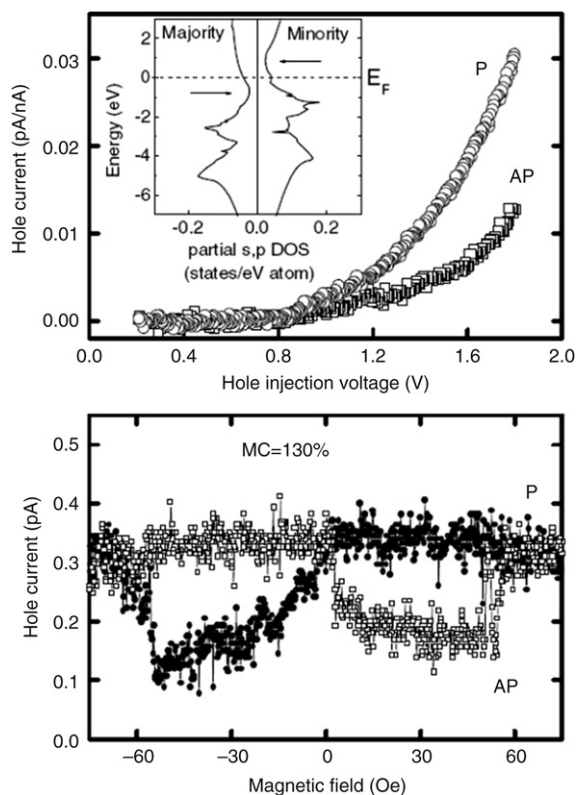


Fig. 10. (Top panel) Hole current as a function of tip bias on Au/Co/Au/NiFe/Au/*p*-Si(001) for P ($H = 100$ Oe) and AP ($H = -30$ Oe) alignment. Inset in this panel shows the *s, p* partial density of states for FCC Co. The arrows indicate the pronounced dips near the top of the *d* bands. (Bottom panel) Hole current as a function of applied magnetic field at a tip bias of 2 V and 10 nA hole current. Reprinted with permission from Ref. [69].

© 2005, American Physical Society.

where elastic scattering dominated. The crossover to positive MC occurred in thicker films where inelastic scattering dominated.

By using BHMM in reverse mode it was found that higher transmission currents could be obtained [71]. In reverse mode, the injected hot electrons from the STM tip decay inelastically via electron–hole pair excitation. The holes created from this process are then transmitted through the sample and enter the valence band of the *p*-type semiconductor [72]. The higher transmission currents made imaging possible on Au/Co/Au/NiFe/Au/*p*-Si samples [71].

Transmission rates of hot electrons/holes in the studies in this chapter are significantly limited by scattering processes within the layers and at metal–metal interfaces due to disorder and band-structure mismatches. Epitaxial base layers may reduce the elastic-scattering rate in the films compared to polycrystalline ones, increasing the BEEM current. In addition, the use of epitaxial thin films as the base layer has proven to be beneficial for improving spatial resolution of BEEM due to the electron focusing effect from the specific band structure of the metal film [19]. BEEM on epitaxial FM thin films requires a complex *in situ* fabrication in a dedicated ultrahigh vacuum (UHV) chamber due to contamination issues. Very few spin transport measurements have been carried out using BEEM-based techniques on epitaxially-grown FM films (see for example Ref. [73]). This, however, leaves much room for further research in this field.

3. Organic thin films and molecules

Organic materials (organics) are chemical compounds consisting primarily of carbon and hydrogen. With the exception of methane and its simple derivatives, most organics have multiple carbon–carbon covalent bonds and can be divided into two

general classes: molecules and polymers (macromolecules composed of repeating structural units). As the basis of all life processes, organics exhibit an extremely large variety of composition, shape and chemical reactivities. The widespread industrial utilization of organics was hallmarked by the fabrication of the first synthetic organic chemical urea (carbamide, $(\text{NH}_2)_2\text{CO}$) by Wöhler in 1828 [74]. Today, artificial organics have become an indispensable part of modern civilization.

Organics have been widely employed as passive components (e.g. device packaging) in the microelectronic industry. One of the earliest applications of organics as *active* components in electronics and optoelectronics was the organic photoconductors developed for xerography in 1960s to overcome issues with amorphous selenium such as inflexibility and poor red light sensitivity [75]. In 1987, Kodak, Inc. first demonstrated an organic light-emitting device (OLED) with high luminosity which triggered tremendous commercial and scientific interest. Today, a large variety of organic electronic and optoelectronic devices are being developed including solar cells and photodetectors [76], chemical sensors [77], charge and data storage devices [78], electroluminescent devices [79], field-effect transistors (FET) [80] and nonlinear optical devices [81]. The main driving factors for replacing conventional inorganic semiconductors with organic semiconductors are their relatively low cost, integrability with established techniques, novel functionality, and flexibility. Molecular electronics is currently considered one possible solution for the continued miniaturization of microelectronics [82].

While OLEDs have found niche markets in small size displays, most of today's organic devices are still in their infant stage, plagued by practical issues such as poor conductivity and carrier mobility, non-optimized charge injection at metal contacts, and relatively short lifetime. Their performance leaves much to be desired compared with their inorganic counterparts. The success of organic-based devices calls for synergy between fundamental research and commercial development. For example, there is a poor understanding of interfacial properties between metal contacts and organics. For optimal carrier injection into organics, close energy alignment between the Fermi level of the contacting metal and the molecular orbital levels of organic molecules is needed. Electron injection into organics is generally more difficult, because it requires low-work-function alkaline metals which are susceptible to oxidation. Theoretical estimation of the energy-level alignment based on the work function difference (the Schottky–Mott rule) usually exhibits a large deviation from experimental results. Typically the energy-level alignments are deduced from conventional macroscopic spectroscopies such as current–voltage (I - V), capacitance–voltage (C - V) and internal photoemission (IPE) which average over a large device active area. These techniques are largely affected by structural inhomogeneities and local defects such as pinholes and impurities. For this reason, a local characterization is highly desirable. BEEM is a valuable tool to study organic electronic structures, charge carrier transport through organic thin films and molecules, and charge injection at metal–organic interfaces on the nanometer scale. In this section, a brief review of the recent progress made in this direction is given.

3.1. BEEM of buried organics

3.1.1. Barrier heights at metal–organic interfaces

To determine barrier heights between metals and organics, a Schottky diode can be made by depositing a metal base overlayer on an organic thin film collector. Troadec et al. studied the interface between Ag and poly(*para*-phenylene) (PPP) polymeric thin films [83]. PPP is a conjugated polymer that emits blue light

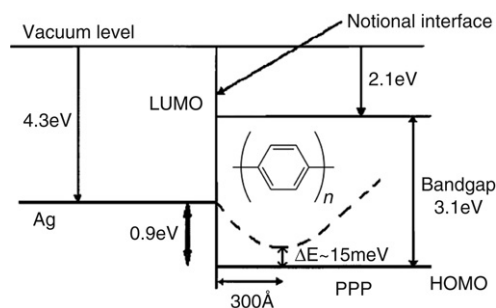


Fig. 11. Energy-level alignment for the Ag/PPP interface following the Schottky–Mott rule. Inset shows the molecular structure of PPP. The dotted line shows the Schottky barrier for hole injection after the image force potential correction. Reprinted with permission from Ref. [83].
© 2005, American Institute of Physics.

with high photoluminescence efficiency. In the form of an infinite polymer, the estimated binding energies for the highest occupied molecular orbital (HOMO) and lowest unoccupied molecular orbital (LUMO) levels of PPP measured with respect to the vacuum level are 5.2 and 2.1 eV, respectively [83]. The Schottky–Mott rule predicts that the Fermi level of Ag is aligned closer to the HOMO level than the LUMO level of PPP. For this reason, Ag is typically used to make injection-limited contacts for hole injection into PPP. A barrier height of 0.9 eV is expected between Ag and PPP as predicted by the Schottky–Mott rule (Fig. 11).

Ballistic hole emission spectroscopy (BHES) found a substantial deviation from this estimate, exhibiting nonzero current below this threshold. Note that the electronic properties (e.g. bandgap) of the PPP material depend on the length of its oligomers [84] and therefore careful structural characterization is needed to quantitatively interpret the BHES spectra. Interestingly, similar to the case of BEEM on inorganic MIS interfaces [85,86], multiple steps were found in the first derivative of the collector current (dI_C/dV_{tip}). However, it is not clear if this derivative technique can be interpreted in the same way as in the case of inorganic MIS structures. For example, Eq. (1) has been used to extract the Schottky barrier height from the raw BHES data. The best fit to their data was obtained with an exponent of $\alpha = 7/2$ and a Schottky barrier height ranging from 0.3 to 0.5 eV. The ballistic hole emission microscopy (BHEM) images exhibited substantial spatial nonuniformity of the interface transparency through the PPP films, with the relatively transparent regions several nanometers in size.

3.1.2. Organic modified metal–semiconductor interfaces

Several groups have adopted hybrid devices using organic molecules to influence and control the characteristics of conventional electronic devices. Compared with other approaches to molecular electronics, hybrid devices have several potential advantages. These include fewer limitations on the choice of molecules and relatively easy integration of molecular functionality with the scalability of established semiconductor technologies. For example, by inserting systematically varying organic molecular monolayers at m–s interfaces, interfacial properties such as the Schottky barrier height can be controlled [87]. Systematic changes in charge transport behavior across the molecularly modified junctions on the macroscale have been found by traditional spectroscopic techniques such as I – V , C – V and IPE [88].

The band profiles of these hybrid devices are somewhat similar to MIS structures extensively studied by BEEM previously, making BEEM an excellent technique to study these hybrid systems on the nanometer scale. In a study by Li et al. on Au/octanedithiol/n-GaAs(001), the molecular layer of 1, 8-octanedithiol [SH(CH₂)₈SH] (C8DT) took the role of an insulator sandwiched between an 8 nm Au electrode and an n-type GaAs substrate [89]. To avoid

Fig. 12. Simultaneous STM (left) and BEEM (right) images of an nTP-Au/octanedithiol/n-GaAs diode (c, d) compared with a reference Au/n-GaAs diode (a, b). The images are obtained at $I_{tip} = 20$ nA and at $V_{tip} = -1.8$ V and -2.1 V, respectively. The scan area is 200×200 nm². The contrast range in the STM images is 5.4 nm and 20 nm for (a) and (c), respectively. The contrast range in the BEEM images is 300 ± 50 pA and 5 pA for (b) and (d), respectively. Reprinted with permission from Ref. [89].
© 2005, American Chemical Society.

possible damage of the molecular layer during the conventional evaporation process, an “nTP” process is used to make the Au base contact. In this process, a Au coated poly(dimethylsiloxane) stamp is used to transfer the contacts to the molecular layer. The presence of the C8DT molecular layer was found to drastically increase the BEEM threshold voltage from -0.9 V to -1.4 V as well as to drastically decrease the overall interface transparency (Figs. 12 and 13). Interestingly, the BEEM current starts to drop for tip biases above -2 V, indicating that the BK model, developed for m–s interfaces, cannot be directly applied. A simple model of the molecular layer as a tunnel barrier of 5 eV with an extra molecular state could reproduce the decrease of BEEM current at high biases. This suggests that the BEEM threshold increase is due to the unoccupied molecular level rather than a change in the m–s band alignment.

In hybrid systems with a discontinuous monolayer of polar molecules at the m–s interface, the dipole field of the molecular layer perpendicular to the surface may affect electron transport through the m–s interface near the embedded pinholes. This is supported by a systematic BEEM study of a discontinuous monolayer of dicarboxylic acid (dC-X) sandwiched between Au and n-GaAs. In this system the dC-X forms an electric dipole layer at the GaAs interface with a perpendicular dipole moment depending on the functional end group “X” (= OCH₃, CN, and CF₃) [90].

For most of the area covered by the molecular monolayer, the BEEM current was found to be very small and the threshold voltage was found to increase to -1.4 V (Fig. 14). The apparent barrier height of 1.4 eV was not fully understood, and was tentatively attributed to photon emission in the metal base as well as electron–hole pair generation in the GaAs substrate [91]. At pinholes where the BEEM current was larger, a lower threshold of -0.95 V was found. The local apparent barrier heights at the pinholes are believed to be modified by the dipole field of surrounding molecules, a proposal supported by electrostatic modeling [92]. This value is consistent with macroscopic I – V , C – V and

